electronics

Article

Optimization Control of Canned Electric Valve Permanent Magnet Synchronous Motor

Qingsong Wu, Wei Li, Guihong Feng and Bingyi Zhang *

School of Electrical Engineering, Shenyang University of Technology, Shenyang 110870, China; wuqingsong@smail.sut.edu.cn (Q.W.); SGD_20230420@smail.sut.edu.cn (W.L.); sygyczx@smail.sut.edu.cn (G.F.)
* Correspondence: wangchao@smail.sut.edu.cn; Tel.: +86-159-4200-1780

Abstract: The traditional canned electric valve consists of an induction motor and a reducer, which need to be matched with the position sensor to achieve precise control of valve position. The position sensor and reducer are not only easily damaged in high-temperature liquids, but also the slip rate of the induction motor is greatly affected by the liquid temperature, which makes it difficult to achieve accurate control. To address the above problems, this paper introduces a new topology of canned electric valve permanent magnet synchronous motor (CEV-PMSM), and a new maximum torque per ampere (MTPA) model is proposed. The new MTPA control equation considering the canned sleeve parameters is derived theoretically. By comparing it with i_d = 0 control and ideal MTPA control strategy, it is proved that the new MTPA model reflects the electric valve operation characteristics more realistically. In order to achieve sensorless control of the electric valve, and to achieve fast response and high-precision control under external disturbances and parameter uncertainties, the proposed control scheme combines sensorless control and two-degree-of-freedom (2-DOF) control. Consequently, the proposed control scheme can effectively improve the static and dynamic performances of the CEV-PMSM, as well as adjust the tracking and anti-disturbance performances independently. Finally, a 2 kW 100 r/min prototype was manufactured and corresponding experiments were conducted to verify the accuracy of the analysis.

Keywords: canned electric valve; permanent magnet synchronous motor; maximum torque per ampere; accurate valve position model; two-degree-of-freedom

Citation: Wu, Q.; Li, W.; Feng, G.; Zhang, B. Optimization Control of Canned Electric Valve Permanent Magnet Synchronous Motor. *Electronics* **2023**, *12*, 2433. https://doi.org/10.3390/electronics12112433

Academic Editor: Sheldon Williamson

Received: 6 April 2023
Revised: 4 May 2023
Accepted: 25 May 2023
Published: 27 May 2023

1. Introduction

As the core component for controlling the flow of fluid in the pipeline, electric valves are widely used in petroleum, metallurgy, environmental protection, water treatment and other industries [1,2]. Under high-temperature and high-pressure conditions, in order to solve the problem of high-temperature dynamic sealing, an integrated electric valve structure is adopted. The integrated structure of the traditional canned electric valve is mainly composed of an induction motor, an independent gear, coupling and a stroke control mechanism. In the limited installation space, the existence of the reducer greatly increases the axial length of the induction motor, which makes it difficult to achieve precise start/stop, and the control accuracy is insufficient. Permanent magnet synchronous motors (PMSM) have the advantages of a high power factor, a high torque density, and strong robustness [3,4], which can meet the harsh working environment and bring new opportunities to the valve field.

Although there are many studies [5,6] describing vector control and direct torque control techniques of permanent magnet motors under different load types, the research in the field of valves is still blank. The valve motor is limited by the size of the space, but it is still hoped that the stator current will be small during operation to reduce heat generation and extend the operating time of high-temperature systems. In order to achieve a larger torque under a smaller current, the MTPA control strategy is regarded as an effective way to improve the ability of output torque [7–13]. The MTPA method is mainly divided into three categories, the look-up table method, the signal injection method, and the formula method. The look-up table method includes the experimental method and the finite element analysis (FEA) method. The look-up table method is complicated and cannot accurately track the MTPA point dynamically. Instead of finding i_q, i_d using polynomials or lookup tables, some studies proposed using a proportional-integral (PI) controller to describe the relationship between i_d and i_q. In reference [7], Angelo Accetta et al. proposed an analytical formulation of the MTPA technique considering the magnetic saturation of the iron core for synchronous reluctance motors, and proved that the proposed technology can increase the torque per ampere. In reference [9], T. Inoue et al. established a MTPA mathematical model of PMSM under the stator flux reference system, and optimized the stator flux for MTPA control based on the motor operating conditions. In reference [10], the dynamic performance of MTPA is obtained by injecting virtual signals. In order to obtain the MTPA control accurately, Ke Li et al. proposed the MTPA method based on variable equivalent parameters, which is intended to accurately solve the MTPA control under different loads [13]. Due to the introduction of a new topology, the MTPA model considering the parameters of the canned sleeve is analytically derived to truly reflect the control performance of the canned electric valve.

To implement vector control, sensors such as optical encoders and resolvers are used to provide a rotor position, which will increase the cost and complexity. However, in some special environments (e.g., dust, underwater, high-temperature, etc.), the application of this type of sensor is limited. The existence of the encoder will reduce the reliability of the electric valve under high temperature and high pressure. Therefore, the sensorless control of PMSM has always been a research hotspot in academia and industry [14,15]. In the control strategy of PMSM, common sensorless control technologies include open-loop estimation based on a mathematical model, the high-frequency signal injection method, the adaptive position observer method, the sliding mode observer method, and the extended Kalman filter. Among them, the accuracy of the open-loop estimation [16] method is greatly affected by the motor parameters. When the motor is running, the motor parameters are always changing dynamically, and the system accuracy is poor. Although the closed-loop estimation methods such as model reference adaptive control [17], state observer method [18], and extended Kalman filters [19] have good performance, they are only suitable for medium- and high-speed industrial applications, since the back EMF is too low and distorted to detect the flux position at low or zero speed. The high-frequency (HF) signal injection method uses its salient pole characteristics to estimate the rotor position under low speed or even at zero speed, which has nothing to do with the back EMF at the fundamental frequency and motor parameters [20–23]. Because this article focuses on the salient-polarity permanent magnet synchronous motor for valves, and the valve system has a low speed, the high-frequency signal injection method is adopted. According to the form of the injected signal, it is divided into voltage signal injection and current signal injection. High-frequency voltage signal injection is divided into rotating voltage injection [20], pulsating sinusoidal voltage injection [21], and square-wave voltage injection [22].

Aiming at the problem that the single-degree-of-freedom controller cannot take into account both tracking and disturbance rejection, reference [24] introduced 2-DOF control to improve the system's disturbance rejection. In order to enhance the current regulation bandwidth and robustness of permanent magnet linear motor, a 2-DOF current controller is designed in reference [25], which is combined with predictive current control (PCC) to obtain better dynamic and static performance. In order to achieve fast response and high-precision control of the bearingless permanent magnet synchronous motor, reference [26] combines the neural network inverse (NNI) method with a 2-DOF internal model controller to enhance system tracking and disturbance rejection performance. Reference [27] combines finite set model predictive control (FS-MPC) with 2-DOF control, and compared with conventional PI controller, it has better dynamic performance and enhances system robustness. In this paper, a 2-DOF control algorithm is used to improve the speed loop, and a position sensorless control system based on 2-DOF control is established.

The remaining contents of this paper are organized as follows. In Section 2, the new topology of CEV-PMSM is proposed, and the integrated structure and operating characteristics are analyzed. In Section 3, as an original contribution, the new MTPA model considering the canned sleeve parameters was developed. In Section 4, sensorless control for CEV-PMSM is implemented. In Section 5, the 2-DOF design of the speed loop PI controller is carried out to improve system robustness. Finally, some conclusions are provided in the last section.

2. Structure and Principle of the New Canned Electric Valve

2.1. Integrated Structure and Characteristics

The integrated structure of the electric valve removes the dynamic sealing structures such as the stuffing box, packing pressure plate, and packing pressure sleeve added in the high-temperature valve. The valve cavity contains a high-temperature, high-pressure liquid medium, so the canned sleeve is introduced into the air gap to form an integrated sealing structure with the housing. If the canned induction motor + reducer structure is adopted, due to the presence of the rotor copper bars, the stator and rotor double-layer canned sleeves are required to isolate high-temperature, high-pressure liquids, which greatly increases the reactive current required to establish the magnetic field, and shortens the running time of the high-temperature system. Moreover, the slip rate is greatly affected by the high-temperature liquid, and it is difficult to ensure accurate position control at low speeds. Special working conditions place higher requirements on the valve motor. The valve motor must have the properties of high temperature and high pressure resistance, accurate tracking and positioning, sealing reliability, and miniaturization advantages.

In order to solve the above problems, this article adopts the integrated structure of CEV-PMSM, as shown in Figure 1. The CEV-PMSM does not need a rotor canned sleeve, which shortens the air gap length and reduces the air gap reluctance. Permanent magnets are used as the excitation source to generate magnetic field instead of stator current armature reaction, so the power factor and torque density are greatly improved. The taper sleeve is used to withstand the pressure on the top of the stator canned sleeve. As the valve stem moves up and down, the valve completes the operation of opening and closing.

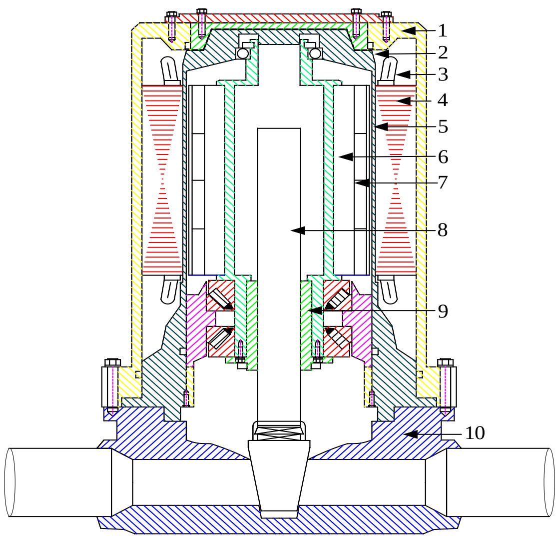

Figure 1. Structure model of the CEV-PMSM. 1. Casing 2. Taper sleeve 3. Winding 4. Stator core 5. Stator canned sleeve. 6. Rotor core 7. Permanent magnets 8. Valve stem 9. Nut 10. Valve body.

2.2. Valve Operation Principle

Among them, Q refers to the flow through the valve, in m^3/h. H refers to the differential pressure before and after the gate, in Pa. Q_1, Q_2 and Q_3 represent the flow percentage, H_1, H_2 and H_3 are the differential pressure at the corresponding flow positions, H_0A, H_0B, H_0C are the flow resistance curves at the corresponding flow positions. Closing the valve gradually from the fully open position, the flow resistance characteristic curve of the pipeline changes from curve H_0A to H_0B, the operating point changes from A to B, and the flow rate decreases from Q_1 to Q_2. When the flow rate of valve reaches 20%, the operating point becomes point C, and the flow resistance characteristic curve is H_0C. Because of the throttling of the fluid, the differential pressure between the front and rear of the gate increases. This differential pressure acts on the gate plate, which makes the stem need a large axial force to drive the gate. h = f(Q) is the differential pressure-flow rate characteristic curve.

The variation of differential pressure with flow rates is illustrated in Figure 2.

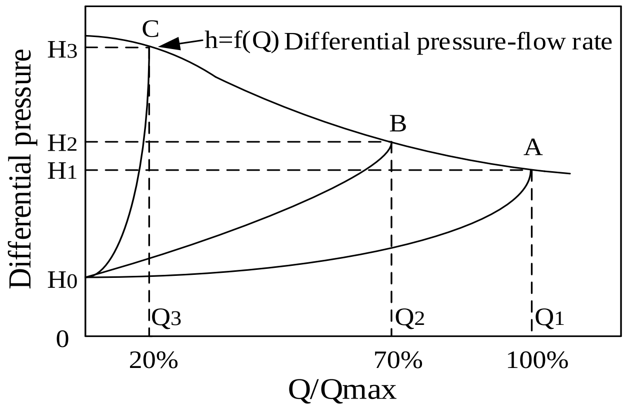

Figure 2. Curve of differential pressure with flow rate.

According to engineering application and space size constraints, Table 1 lists the main parameters of the CEV-PMSM.

Table 1. Technical requirements for canned electric valve.

Parameter	CEV-PMSM
Power/kW	2
Core length/mm	180
Stator outer diameter/mm	175
Stator inner diameter/mm	120
Rotor outer diameter/mm	118
Rotor inner diameter/mm	60
Effective mass/kg	26.03
Rated torque/(N·m)	191
Torque density/(N·m/kg)	7.337
Speed/rpm	100
Thermal load/(A^2/mm^3)	1300.3
Radial space dimensions/mm	200
Operating duration/s	30

The control analysis flow chart is shown in Figure 3. Whether the new MTPA control or the sensorless control with 2-DOF is adopted, the cycle is terminated when the control performance required by the electric valve system is satisfied.

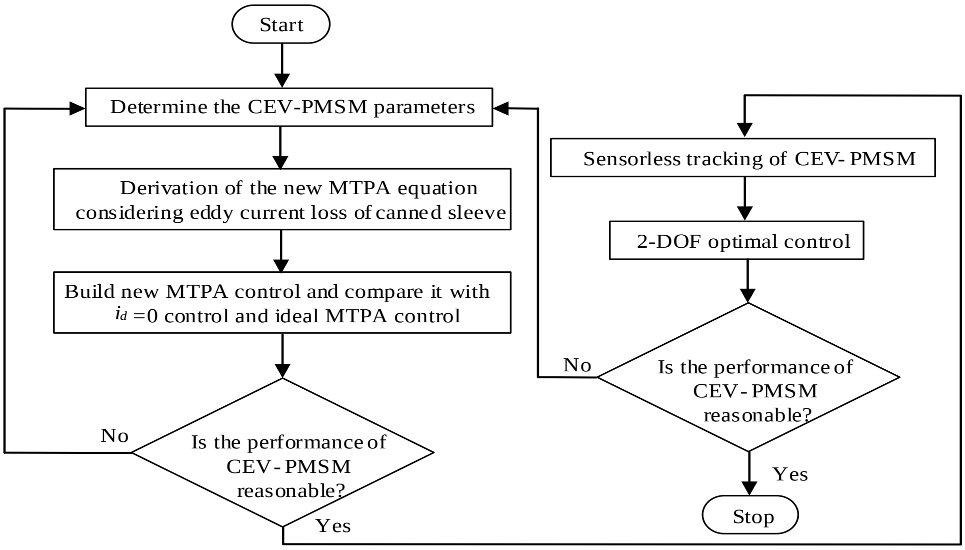

Figure 3. Analysis flow chart of the new CEV-PMSM.

In this paper, we establish the new MTPA model considering the eddy current loss resistance of the canned sleeve. On this basis, the position sensorless algorithm is combined with the 2-DOF control to achieve optimal control of CEV-PMSM. Figure 4 is the CEV-PMSM model diagram, adopting the 10-pole/24-slot combination.

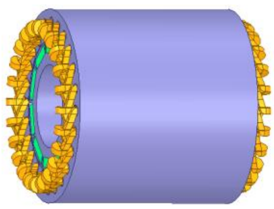

Figure 4. 10-pole/24-slot CEV-PMSM model.

3. New MTPA Control Model for CEV-PMSM System

3.1. Description of the Equivalent Circuit

Based on the *d*-*q* axis equivalent circuit model of the traditional PMSM, the proposed equivalent model is shown in Figure 5. The equivalent circuit includes the canned sleeve eddy current loss resistance R_{can}, which is calculated by finite element analysis at the high temperature of 200 °C. R_{can} has a great influence on the performance of CEV-PMSM, and the speed of motor and the thickness of the stator canned sleeve have an influence on its value. Because of its importance, the presence of R_{can} cannot be ignored in the MTPA model.

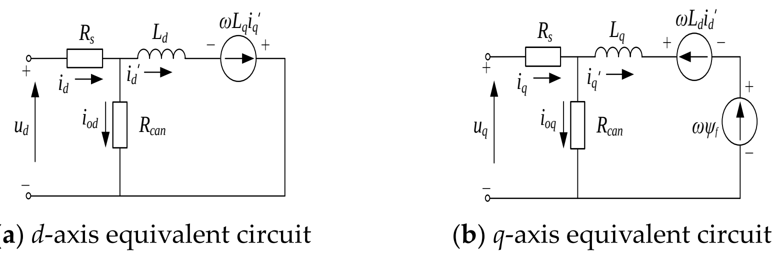

Figure 5. *d*-*q* axis equivalent circuits in the rotor reference frame of CEV-PMSM.

Where: i_d and i_q are the *d*- and *q*-axes components of the stator current; L_d and L_q are the *d*- and *q*-axes inductances; i_d' and i_q' are the *d*- and *q*-axes inductances branch current;

Ψ_f is the magnet flux linkage; R_s is the resistance of the stator; R_{can} is the eddy current loss resistance of the canned sleeve; ω is the electrical speed of rotor.

Although the traditional *d*-*q* axis equivalent circuit can reflect the performance changes of conventional permanent magnet motors, it cannot explain the pulsation of torque and speed during the experiment of canned electric valve motors.

3.2. Mathematical Model

The equivalent circuit of the *d*-*q* axis is shown in Figure 5, and the corresponding voltage equation can be obtained as follows:

$$\begin{cases} u_d = R_s i_d + L_d \frac{di_d{}'}{dt} - \omega L_q i_q{}' \\ u_q = R_s i_q + L_q \frac{di_q{}'}{dt} + \omega L_d i_d{}' + \omega \psi_f \end{cases} \tag{1}$$

$$\begin{cases} u_d = R_s i_d + R_{can} i_{od} \\ u_q = R_s i_q + R_{can} i_{oq} \end{cases} \tag{2}$$

d-*q* axis flux linkage equation can be calculated as follows:

$$\begin{cases} \psi_d = L_d i_d{}' + \psi_f \\ \psi_q = L_q i_q{}' \end{cases} \tag{3}$$

The rotor motion equation is expressed as follows:

$$T_e = J \frac{d\omega_r}{dt} + B_m \omega_r + T_L \tag{4}$$

The corresponding generated electromagnetic torque is given by:

$$T_e = \frac{3}{2} p_n \left[\psi_f \cdot i_q{}' + \left(L_d - L_q \right) \cdot i_d{}' \cdot i_q{}' \right] \tag{5}$$

where: ψ_d, ψ_q are the *d*- and *q*-axes flux components in the rotor reference frame; J_m is the moment of inertia; B_m is the viscous damping coefficient; ω_r is the mechanical angular velocity of the rotor; p_n is the number of pole pairs.

The new voltage equation has been derived by substituting (1) and (2) into the following voltage equation, accounting the influence of the canned sleeve parameters on the circuit equation:

$$\begin{cases} u_d & = R_s i_d + \frac{\omega^2 L_d L_q R_{can}}{\omega^2 L_d L_q + R_{can}{}^2} i_d - \frac{\omega L_q R_{can}{}^2}{\omega^2 L_d L_q + R_{can}{}^2} i_q \\ & + \frac{\omega^2 \psi_f R_{can} L_q}{\omega^2 L_d L_q + R_{can}{}^2} \\ u_q & = R_s i_q + \frac{\omega L_d R_{can}{}^2}{\omega^2 L_d L_q + R_{can}{}^2} i_d + \frac{\omega^2 L_d L_q R_{can}}{\omega^2 L_d L_q + R_{can}{}^2} i_q \\ & + \frac{\omega \psi_f R_{can}{}^2}{\omega^2 L_d L_q + R_{can}{}^2} \end{cases} \tag{6}$$

In the steady state stage, when the motor runs at a constant speed, the voltage across the inductances are 0, and the following assumptions are made:

$$\frac{\omega^2 \cdot L_d \cdot L_q}{R_{can}{}^2} << 1 \quad \text{and} \quad \frac{R_s}{R_{can}} << 1 \tag{7}$$

The steady-state *d*- and *q*-axis equations of the CEV-PMSM in the rotor reference frame are given in:

$$\begin{pmatrix} u_d \\ u_q \end{pmatrix} = \begin{pmatrix} R_s + \frac{\omega^2 \cdot L_d \cdot L_q}{R_{can}} & -\omega \cdot L_q \\ \omega \cdot L_d & R_s + \frac{\omega^2 \cdot L_d \cdot L_q}{R_{can}} \end{pmatrix} \cdot \begin{pmatrix} i_d \\ i_q \end{pmatrix} + \begin{pmatrix} \frac{\omega^2 \cdot L_q \cdot \psi_f}{R_{can}} \\ \omega \psi_f \end{pmatrix} \tag{8}$$

$$\begin{cases} i_d{}' = \frac{R_{can}{}^2 i_d + \omega L_q R_{can} i_q - \omega^2 \psi_f L_q}{R_{can}{}^2 + \omega^2 L_d L_q} \\ i_q{}' = \frac{R_{can}{}^2 i_q - \omega L_d R_{can} i_d - \omega \psi_f R_{can}}{R_{can}{}^2 + \omega^2 L_d L_q} \end{cases} \tag{9}$$

where $H = \left(R_{can}{}^2 + \omega^2 L_d L_q\right) / R_{can}{}^2$

$$\begin{pmatrix} i_d{}' \\ i_q{}' \end{pmatrix} = \frac{1}{H} \cdot \begin{pmatrix} 1 & \frac{\omega \cdot L_q}{R_{can}} \\ -\frac{\omega \cdot L_d}{R_{can}} & 1 \end{pmatrix} \cdot \begin{pmatrix} i_d \\ i_q - \frac{\omega \cdot \psi_f}{R_{can}} \end{pmatrix} \tag{10}$$

3.3. MTPA Control Equation

In order to minimize the effects of joule losses in the stator windings and maximize the electromagnetic torque, maximum torque per ampere (MTPA) techniques have been developed. The MTPA control problem can be formulated as the problem of minimizing the amplitude of the stator current, and the objective function is to maximize the electromagnetic torque under constraint conditions.

$$\begin{cases} \min \quad I = \sqrt{i_d{}^2 + i_q{}^2} \\ subject\ to \ \ T_e = \frac{3}{2} p_n \left[\psi_f \cdot i_q{}' + \left(L_d - L_q\right) \cdot i_d{}' \cdot i_q{}' \right] \end{cases} \tag{11}$$

Using Lagrange's theorem in mathematics, establish an auxiliary function F, and seek its extreme value:

$$F = i_d{}^2 + i_q{}^2 + \lambda \left[\frac{3}{2} p_n \psi_f i_q{}' + \frac{3}{2} p_n (L_d - L_q) i_d{}' i_q{}' - T_e \right] \tag{12}$$

Which is obtained by substituting (9) into (12) yields:

$$F = i_d{}^2 + i_q{}^2 + \lambda \left[\begin{array}{c} \frac{3}{2} p_n \psi_f \frac{i_q - \frac{\omega L_d}{R_{can}} i_d - \frac{\omega \psi_f}{R_{can}}}{1 + \frac{\omega^2 L_d L_q}{R_{can}{}^2}} + \frac{3}{2} p_n \left(L_d - L_q\right) \\ \cdot \frac{\left(i_q - \frac{\omega L_d}{R_{can}} i_d - \frac{\omega \psi_f}{R_{can}}\right)\left(i_d + \frac{\omega L_q}{R_{can}} i_q - \frac{\omega^2 L_q \psi_f}{R_{can}{}^2}\right)}{\left(1 + \frac{\omega^2 L_d L_q}{R_{can}{}^2}\right)^2} \end{array} \right] \tag{13}$$

where: λ is the Lagrangian multiplier. The MTPA condition is satisfied when all partial derivatives of (14) are zero.

$$\frac{\partial F}{\partial i_d} = 0 \ \ \frac{\partial F}{\partial i_q} = 0 \ \ \frac{\partial F}{\partial \lambda} = 0 \tag{14}$$

$$\begin{cases} \frac{\partial F}{\partial i_d} = 2 i_d + \lambda \left\{ -\frac{\omega L_d}{R_{can}} A + B \left[\begin{array}{c} -\frac{\omega L_d}{R_{can}} \left(i_d + \frac{\omega L_q}{R_{can}} i_q - \frac{\omega^2 \psi_f L_q}{R_{can}} \right) \\ + \left(i_q - \frac{\omega L_d}{R_{can}} i_d - \frac{\omega \psi_f}{R_{can}} \right) \end{array} \right] \right\} = 0 \\ \frac{\partial F}{\partial i_q} = 2 i_q + \lambda \left\{ A + B \left[\begin{array}{c} \left(i_d + \frac{\omega L_q}{R_{can}} i_q - \frac{\omega^2 \psi_f L_q}{R_{can}{}^2} \right) \\ + \frac{\omega L_q}{R_{can}} \left(i_q - \frac{\omega L_d}{R_{can}} i_d - \frac{\omega \psi_f}{R_{can}} \right) \end{array} \right] \right\} = 0 \end{cases} \tag{15}$$

$$\begin{cases} A = \frac{\frac{3}{2}p_n\psi_f}{1+\frac{\omega^2 L_d L_q}{R_{can}{}^2}} & B = \frac{\frac{3}{2}p_n(L_d-L_q)}{\left(1+\frac{\omega^2 L_d L_q}{R_{can}{}^2}\right)^2} \\ C = -\frac{2\omega L_d}{R_{can}}B & D = B\left(1-\frac{\omega^2 L_d L_q}{R_{can}{}^2}\right) \\ E = B\frac{\omega\psi_f}{R_{can}}\left(\frac{\omega^2 L_d L_q}{R_{can}{}^2}-1\right)-\frac{\omega L_d}{R_{can}}A \\ K = \frac{2\omega L_q}{R_{can}}B & G = A-\frac{2\omega^2 L_q\psi_f}{R_{can}{}^2}B \end{cases} \tag{16}$$

From Equation (16), we can know that the values of parameters A–G are changing with the speed, which laterally reflects the influence of canned sleeve eddy current loss resistance by speed.

Through algebraic manipulation of (15) and (16), the following relationship between i_d, i_q and λ can be found:

$$\begin{cases} \lambda = -\frac{2i_d}{Ci_d+Di_q+E} \\ i_q = \frac{i_d(Di_d+Ki_q+G)}{Ci_d+Di_q+E} \end{cases} \tag{17}$$

The relationship between MTPA currents can be obtained by using quadratic formula. Between the two solutions, the one with a minus sign gives a reasonable solution for the MTPA condition. Thus, the *d*-axis current calculation equation is as follows:

$$i_d = \frac{-[(K-C)i_q+G]-\sqrt{[(K-C)i_q+G]^2+4Di_q(E+Di_q)}}{2D} \tag{18}$$

3.4. Analysis of the New MTPA Control System

A. Comparison with i_d = 0 control model

Figure 6 shows the new MTPA model of the system, built on the Simulink simulation platform in MATLAB R2021b software. The parameter settings of the CEV-PMSM are shown in Table 2.

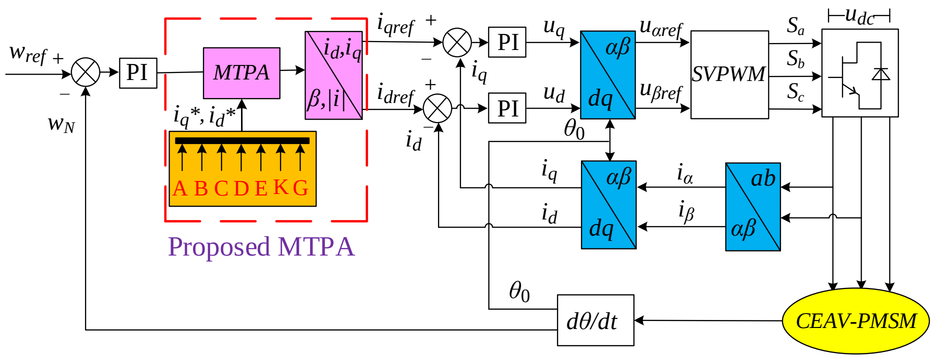

Figure 6. Vector control block diagram of the new MTPA model.

Figure 6 is the vector control block diagram of CEV-PMSM, which is the new MTPA model considering the canned sleeve parameters. The control system employs double closed-loop control of the speed loop and current loop. Based on the ideal MTPA control module, a new MTPA model considering the eddy current loss of the canned sleeve is proposed, as shown in the red block diagram. The parameters A, B, C, D, E, K, and G are the derivation results of the new MTPA control equation after considering the eddy current loss of the canned sleeve. Through the parameters A, B, C, D, E, K, and G, the functional relationship between i_d and i_q in the new MTPA control can be determined.

Table 2. Performance parameters.

Parameter Symbol	Parameter Name	Value
R_s	Stator resistance/Ω	15.652
L_d	*d*-axis inductance/H	0.210458
L_q	*q*-axis inductance/H	0.253205
ψ_f	Permanent magnet flux/Wb	1.435
ω_N	Rated speed/rpm	100
p	Number of pole pairs	5
R_{can}	Canned sleeve eddy current resistance/Ω	360
J	Moment of inertia/(kg·m^2)	0.026723
T_{eN}	Rated torque/Nm	191

The CEV-PMSM starts at rated load. When it runs to 0.4 s, the torque setpoint suddenly changes to 1.2 times the rated torque. When it runs to 0.7 s, the torque setpoint suddenly changes to 0.8 times the rated torque. Observe the operating performance of the CEV-PMSM under the new MTPA control strategy and compare it with the i_d =0 control strategy to verify effectiveness of the new MTPA control model. The reference speed of the simulation process is given as the rated speed of 100 r/min, and the simulation results are analyzed.

It can be observed from Figure 7 that when the rated load is started, the overshoot of the MTPA control strategy is very small. When it runs overload operation at 0.4 s, the amplitude of speed drop is relatively large under the i_d = 0 strategy; under the new MTPA control strategy, the dynamic response speed is fast, reaching the overload torque within 0.1 s and running stably. In light load operation at 0.7 s, the new MTPA control also has a better dynamic response.

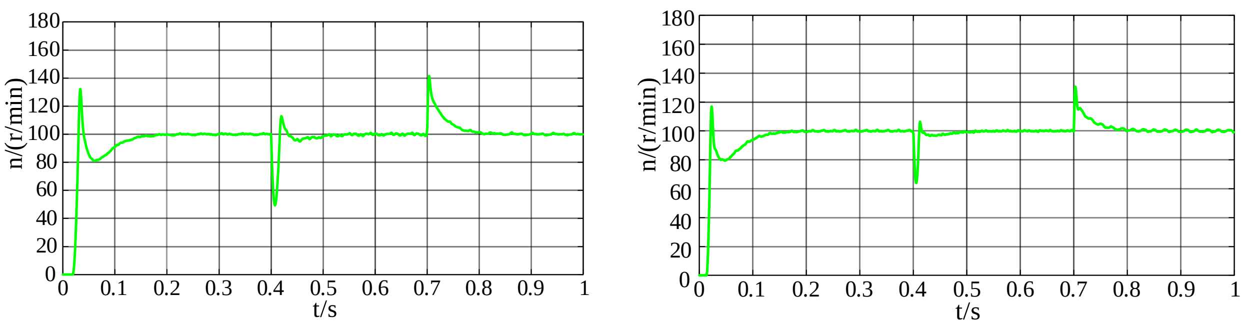

(**a**) $i_d = 0$ (**b**) new MTPA

Figure 7. Speed curve change of the new MTPA and i_d = 0 control strategies.

Figures 8 and 9 are the comparison diagrams of the *d*-*q* axis current waveforms of new MTPA and i_d = 0 control strategies under different loads. At rated load, under the i_d = 0 control strategy, the *q*-axis current amplitude fluctuates between 16.5 A and 18.5 A, and the center value is about 17.5 A. However, the d-axis current fluctuates between −1.5 A and 1.5 A. The value is zero; when using MTPA control at rated load, the *q*-axis current amplitude fluctuates between 13.6 A and 15.8 A, the center value is 14.7 A. However, the d-axis current fluctuates between −4.2 A and −7 A, and the center value is −5.6 A. In the same way, the two control strategies under overload and light load are applicable to CEV-PMSM, and the new MTPA control strategy can still achieve excellent performance.

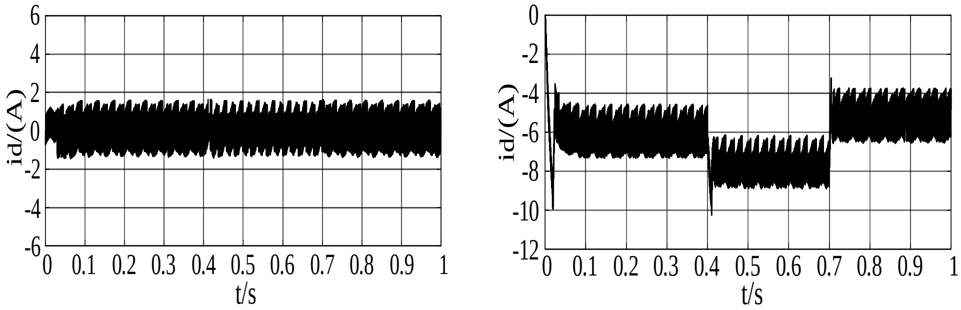

(**a**) i_d =0 (**b**) new MTPA

Figure 8. Comparison of *d*-axis current waveform between the new MTPA and i_d = 0 control strategies.

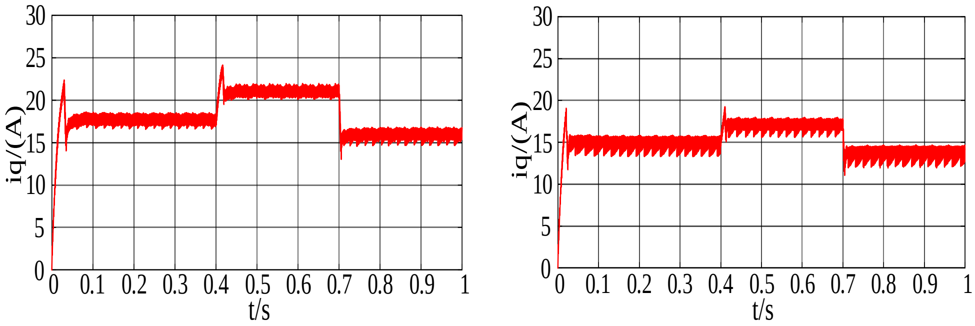

(**a**) i_d = 0 (**b**) new MTPA

Figure 9. Comparison of *q*-axis current waveform between the new MTPA and i_d = 0 control strategies.

Figure 10 shows that when CEV-PMSM is under the 0.8 times rated torque, the stator current required by the two control strategies is not much different. As the load increases, the stator current required by the new MTPA control strategy is smaller relative to i_d = 0.

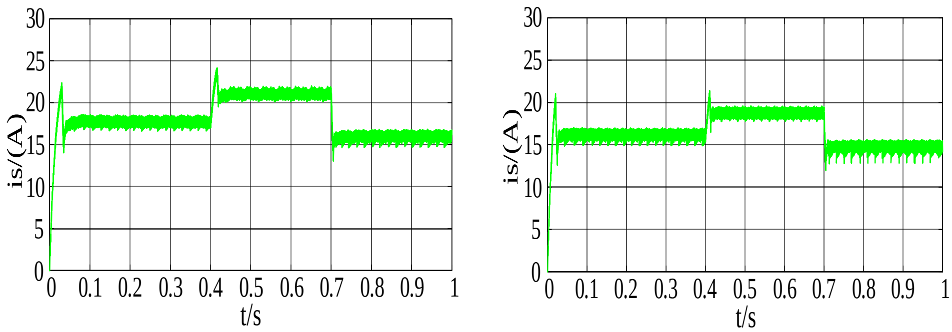

(**a**) i_d = 0 (**b**) new MTPA

Figure 10. Comparison of stator current waveform between the new MTPA and i_d = 0 control strategies.

Figure 11 shows the mechanical torque waveform change of CEV-PMSM. The i_d = 0 control strategy reaches the rated torque in 0.07 s, while the new MTPA strategy reaches the rated torque in 0.04 s without overshoot. When the overload torque is added suddenly at 0.4 s, the i_d = 0 strategy will resume stable operation within 0.04 s, while it only takes 0.02 s under the MTPA strategy. For the new model CEV-PMSM, the new MTPA strategy has a good dynamic response performance.

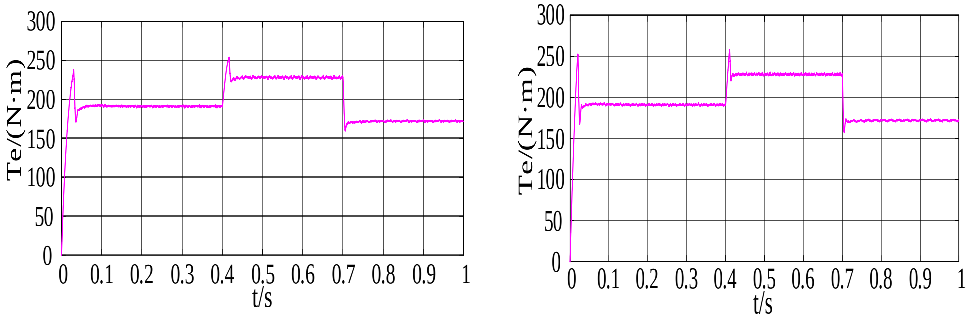

(**a**) $i_d = 0$ (**b**) new MTPA

Figure 11. Comparison of mechanical torque waveform between the new MTPA and $i_d = 0$ control strategies.

It can be observed from Figure 12 that the three-phase current waveform under the new MTPA strategy is significantly smaller than the $i_d = 0$ strategy. When the rated torque is suddenly increased by 1.2 times at 0.4 s, the actual current value under the new MTPA strategy can also be quickly tracked to the given value, there is basically no impact error, and the waveform is almost without distortion.

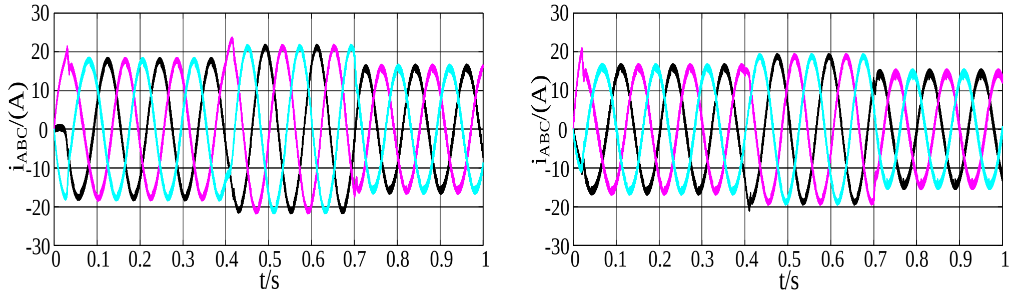

(**a**) i_d =0 (**b**) new MTPA

Figure 12. Three-phase current waveform under the new MTPA and $i_d = 0$ control strategies.

B. Comparison with ideal MTPA model

In order to compare the variability of the MTPA model under non-ideal and ideal operating conditions, we explore the effect of canned sleeve parameters on system performance, and further analyze the changes in system performance during overload and overspeed stages. The load torque suddenly changes to 1.2 times of the rated torque at 0.4 s, and the speed becomes 1.2 times of the rated speed at 0.8 s.

Figure 13 shows that the parameters of the canned sleeve have a certain influence on the ripple torque. The canned sleeve causes the torque harmonic content to increase and the torque ripple to become larger. The change of torque is influenced by the stator equivalent current, so the stator current needs to be analyzed.

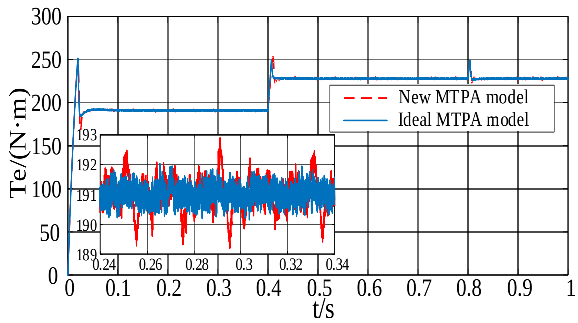

Figure 13. Torque waveform curve.

Figure 14 shows that the canned sleeve parameters increase the harmonic content of the stator current. The stator harmonic content is small when there is no canned sleeve, and the new model accurately reflects the influence of the eddy current loss of the canned sleeve on the current performance.

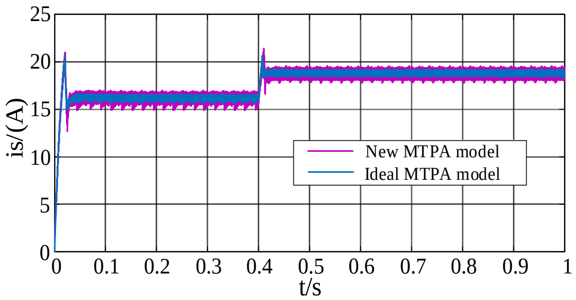

Figure 14. Stator current waveform curve.

It can be observed from the equivalent circuit in Figure 5 that the existence of the canned sleeve causes the *d*-*q* axis circuit to have a branch, which is different from the ideal equivalent circuit. I_d and i_q shunt to the canned eddy current resistance, resulting in i_d, i_q current fluctuations, so the stator current fluctuates.

Fourier decomposition of the phase current waveforms are shown in Figure 15. Since the fundamental current is one, this figure shows the percentage of each harmonic current to the fundamental current.

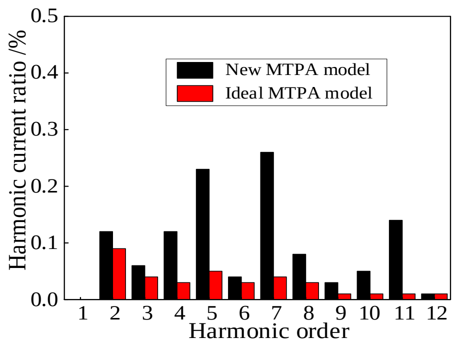

Figure 15. Current harmonic analysis diagram.

After the canned sleeve is introduced, the harmonic content of the stator current increases significantly, indicating that the influence of canned sleeve eddy current loss on the system cannot be ignored, and the specific harmonic components need to be explored. As can be seen from Figure 15, the new MTPA model has a higher harmonic component, and the canned sleeve parameters greatly affect the 5th and 7th harmonic components.

4. Sensorless Tracking of CEV-PMSM

In order to achieve sensorless control of CEV-PMSM in the low-speed range, this paper adopts a rotating high-frequency voltage injection method. Based on the salient pole effect of the CEV-PMSM, a high-frequency rotating voltage is injected into the stationary coordinate system, and the high-frequency response current signal is extracted by a filter. Finally, the rotor position can be detected by demodulating the negative phase sequence component.

4.1. Mathematical Model of CEV-PMSM under High-Frequency Excitation

Under the excitation of the high-frequency rotating voltage signal, the stator resistance Rs can be neglected compared to the high-frequency reactance. At this time, the model of the CEV-PMSM under high-frequency excitation can be equivalent to a pure inductance model.

Under high-frequency excitation, the relationship between voltage and high-frequency reactance is:

$$\begin{bmatrix} u_{di} \\ u_{qi} \end{bmatrix} = \begin{bmatrix} L_d P & 0 \\ 0 & L_q P \end{bmatrix} \begin{bmatrix} i_{di} \\ i_{qi} \end{bmatrix} \tag{19}$$

The high-frequency circuit model is shown in Figure 16.

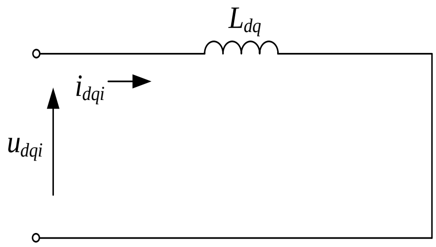

Figure 16. High-frequency circuit of CEV-PMSM.

In order to accurately estimate the position of the CEV-PMSM, the relationship between the estimated rotor synchronous rotation coordinate system $\hat{d}$-$\hat{q}$ and the actual rotor synchronous rotation coordinate system d-q is established, as shown in Figure 17.

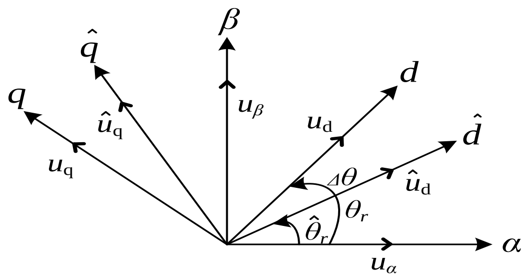

Figure 17. Relation diagram of two-phase coordinate system.

Where: u_{di}, u_{qi}, i_{di}, and i_{qi} are the HF voltages and currents, respectively; P is a derivative operator; θ_r is the actual rotor position angle; $\hat{\theta}_r$ is the estimated rotor position; $\Delta\theta$ is the difference between the actual rotor position angle and the estimated rotor position angle.

$$\begin{bmatrix} u_{\alpha i} \\ u_{\beta i} \end{bmatrix} = \begin{bmatrix} \cos\theta_r & \sin\theta_r \\ -\sin\theta_r & \cos\theta_r \end{bmatrix}^{-1} \begin{bmatrix} L_d P & 0 \\ 0 & L_q P \end{bmatrix} \begin{bmatrix} \cos\theta_r & \sin\theta_r \\ -\sin\theta_r & \cos\theta_r \end{bmatrix} \begin{bmatrix} i_{\alpha i} \\ i_{\beta i} \end{bmatrix} \tag{20}$$

$$\begin{bmatrix} u_{\alpha i} \\ u_{\beta i} \end{bmatrix} = \begin{bmatrix} L + \Delta L\cos 2\theta_r & \Delta L\sin 2\theta_r \\ \Delta L\sin 2\theta_r & L - \Delta L\cos 2\theta_r \end{bmatrix} \cdot P \begin{bmatrix} i_{\alpha i} \\ i_{\beta i} \end{bmatrix} \tag{21}$$

Here, $L = (L_d + L_q)/2$ is the average inductance, and $\Delta L = (L_d - L_q)/2$ is the half-difference inductance.

Define the inductance matrix as:

$$L_{\alpha\beta} = \begin{bmatrix} L + \Delta L\cos 2\theta_r & \Delta L\sin 2\theta_r \\ \Delta L\sin 2\theta_r & L - \Delta L\cos 2\theta_r \end{bmatrix} \tag{22}$$

It can be observed from Equation (22) that the inductance matrix $L_{\alpha\beta}$ contains rotor position information, and the switching frequency of the inverter is generally 10 kHz. In order to ensure the sine of the high-frequency voltage signal, the frequency ωi of the injected high-frequency voltage signal is generally 0.5–2 kHz.

4.2. HF Rotating Voltage Injection

In the two-phase stationary coordinate system, a high-frequency rotating voltage is injected into the CEV-PMSM. The injected voltage can be described as:

$$u_{\alpha\beta in} = \begin{bmatrix} u_{\alpha i} \\ u_{\beta i} \end{bmatrix} = \begin{bmatrix} V_i \cos \omega_i t \\ V_i \sin \omega_i t \end{bmatrix} \tag{23}$$

where: V_i, ω_i represent the amplitude and the frequency of the injected vector voltage, respectively.

According to the high-frequency mathematical model of CEV-PMSM in the two-phase stationary coordinate system, the high-frequency response current equation in the coordinate system can be expressed as:

$$\frac{d}{dt}\begin{bmatrix} i_{\alpha i} \\ i_{\beta i} \end{bmatrix} = \begin{bmatrix} L + \Delta L \cos 2\theta_r & \Delta L \sin 2\theta_r \\ \Delta L \sin 2\theta_r & L - \Delta L \cos 2\theta_r \end{bmatrix}^{-1} \begin{bmatrix} V_i \cos \omega_i t \\ V_i \sin \omega_i t \end{bmatrix} \tag{24}$$

$$\begin{bmatrix} i_{\alpha i} \\ i_{\beta i} \end{bmatrix} = \frac{V_i L}{\omega_i (L^2 - \Delta L^2)} \begin{bmatrix} \sin \omega_i t \\ -\cos \omega_i t \end{bmatrix} + \frac{V_i \Delta L}{\omega_i (L^2 - \Delta L^2)} \begin{bmatrix} \sin(2\theta_r - \omega_i t) \\ -\cos(2\theta_r - \omega_i t) \end{bmatrix} \tag{25}$$

Transforming the above formula to the stationary coordinate system, the expression is:

$$i_{\alpha\beta i} = I_p * \begin{bmatrix} \sin \omega_i t \\ -\cos \omega_i t \end{bmatrix} + I_n * \begin{bmatrix} \sin(2\theta_r - \omega_i t) \\ -\cos(2\theta_r - \omega_i t) \end{bmatrix} \tag{26}$$

It can be noticed from Equation (26) that the high-frequency current contains both positive and negative sequence components. The first component, called the positive-sequence component I_p, is proportional to the average inductance, but does not contain information on the rotor position θ_r. The second component, called negative-sequence component I_n, is proportional to the half difference inductance and contains information on the rotor position θ_r.

$$I_p = \frac{V_i L}{\omega_i (L^2 - \Delta L^2)} \tag{27}$$

$$I_n = \frac{V_i \Delta L}{\omega_i (L^2 - \Delta L^2)} \tag{28}$$

Therefore, it is necessary to filter out the fundamental frequency current, low-order harmonic current, PWM switching frequency harmonic current, and positive phase sequence high-frequency current in the terminal current of CEV-PMSM. Finally, the rotor position can be detected by demodulating the negative phase sequence component.

4.3. Synchronous Frame Filter (SFF)

Conventional filtering methods use band-pass filters and band-stop filters, which will cause problems such as larger phase shift and amplitude attenuation. In order to avoid the above problems, synchronous frame filters are used in this article.

The SFF transforms the high-frequency signal quantity (α, β) in other coordinate systems into the synchronous coordinate system (d-q) with the same frequency as the high-frequency signal. At this time, the current component of the positive phase sequence will become a direct component, and the component of the negative phase sequence will become a high-frequency component. After that, a high-pass filter is used to eliminate the positive phase sequence component. Figure 18 shows the block diagram of the SFF.

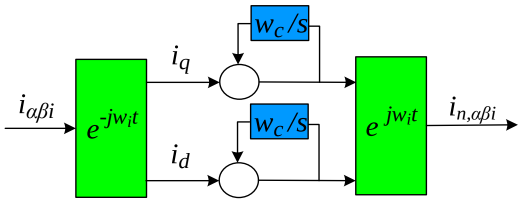

Figure 18. Block diagram of the SFF.

Where ω_c represents the carrier frequency.

After filtering, the remaining signal is the negative phase sequence high-frequency current component, which is a useful signal that can be used to track the salient pole, and its vector expression is:

$$i_{n,\alpha\beta i} = I_n * \begin{bmatrix} \sin(\omega_i t - 2\theta_r) \\ -\cos(\omega_i t - 2\theta_r) \end{bmatrix} \tag{29}$$

4.4. Rotor Position Extraction by Heterodyne Method

The phase angle modulation is found by the heterodyne method to demodulate the negative phase sequence component, and obtain the tracking error signal, which can be expressed as:

$$\begin{aligned} e &= i_{\alpha in}\cos(2\hat{\theta}_r - \omega_i t) - i_{\beta in}\sin(2\hat{\theta}_r - \omega_i t) \\ &= i_{in}\sin 2(\hat{\theta}_r - \theta_r) \approx 2i_{in}\cdot(\hat{\theta}_r - \theta_r) = 2i_{in}\cdot\Delta\theta \end{aligned} \tag{30}$$

As long as the tracking error signal $\Delta\theta$ is adjusted to approach zero, it can be ensured that the estimated rotor position angle converges to the actual rotor position angle. After this error signal passes through the loop filter of the first-order integral nature, the estimated value of the rotation speed can be obtained, and the estimated value of the rotor magnetic pole position can be obtained by further integrating the rotation speed.

4.5. Zero Lag Position Tracking Observer

Estimate the rotor pole position from the negative sequence component, and use the Romberg observer to observe the rotor pole position.

The rotor position tracking observer can obtain an error signal tending to zero, as illustrated in Figure 19. Since the position observer introduces the torque variable, the observer can achieve accurate observation without phase lag. According to the rotor position observer in Figure 19, the transfer function between the rotor position and the estimated position is obtained, as shown in Equation (31).

$$\frac{\hat{\theta}_r}{\theta_r} = \frac{Js^3 + K_d s^2 + K_p s + K_i}{\hat{J}s^3 + K_d s^2 + K_p s + K_i} \tag{31}$$

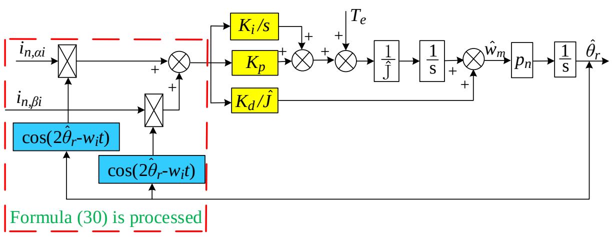

Figure 19. Rotor position observer.

4.6. Analysis of Sensorless Simulation

According to the above theory, the Simulink model shown in Figure 20 is established.

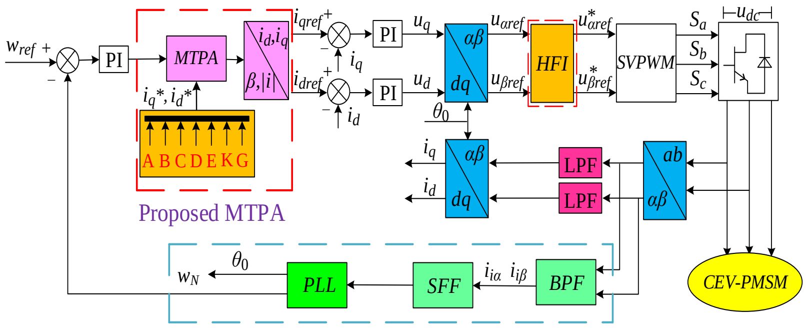

Figure 20. Block diagram of sensorless system based on rotating high-frequency voltage signal injection.

Figure 21 shows the speed tracking waveform at no load, and the speed changes to 150 r/min at 0.5 s. It can be noticed that regardless of the speed-up stage or the rated speed, the actual speed and the estimated speed have good consistency. The control algorithm of high-frequency signal injection enables the motor to track the target speed in real time, which can meet the accuracy requirements of the CEV-PMSM system.

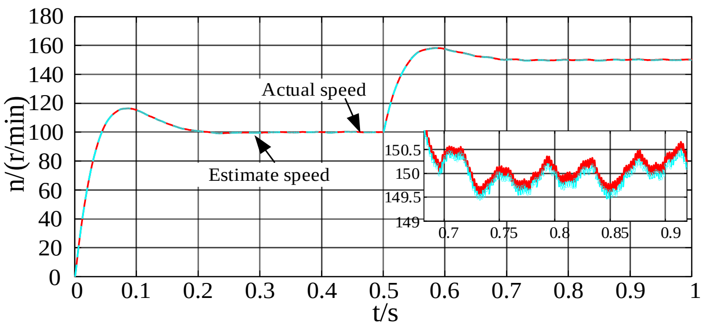

Figure 21. No-load speed tracking waveform.

Figure 22 shows the speed estimation error curve. The speed estimation error has a larger value during the speed-up stage, and the speed estimation error gradually decreases as the speed runs stably. In general, the speed estimation error amplitude is small, and the tracking performance is better.

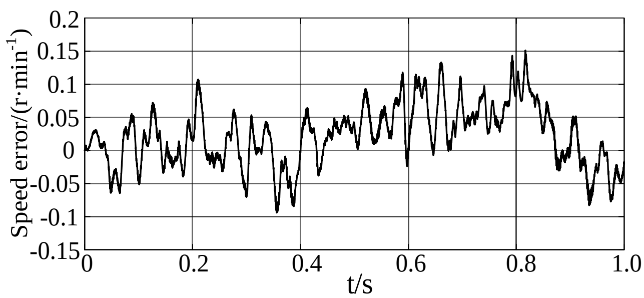

Figure 22. Speed estimation error curve.

Figure 23a is the contrast waveform between the actual angle and the estimated angle when the motor speed changes suddenly. Figure 23b is a partial enlarged view of the rotor position. It can be seen that the estimated speed and the actual speed are in good agreement.

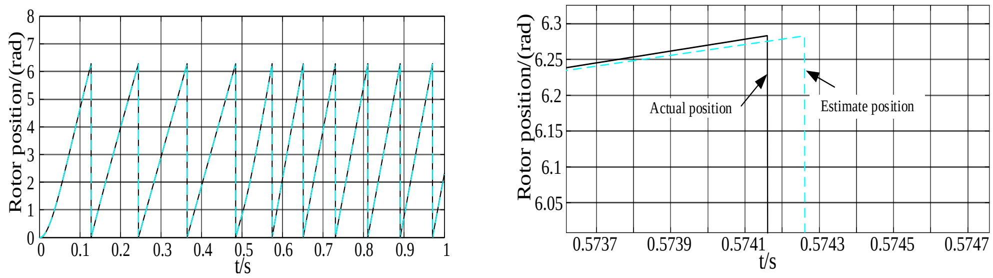

(**a**) Rotor position tracking diagram (**b**) Partial enlarged view of rotor position

Figure 23. Rotor position curve.

According to Figure 24, the position estimation error diagram shows that the rotor position error is less than about 0.01 rad. As the speed stabilizes, the rotor position estimation error is gradually reduced, and the tracking performance is good.

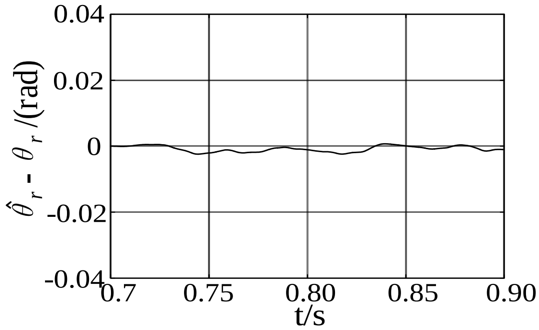

Figure 24. Rotor position estimation error curve.

Figure 25a,b show the actual value and estimated value of the rotor position when the actual speed changes from 100 r/min to −100 r/min according to the slope law. When it reverses suddenly at 0.3 s, the rotor position tracking performance is still maintained during the deceleration process.

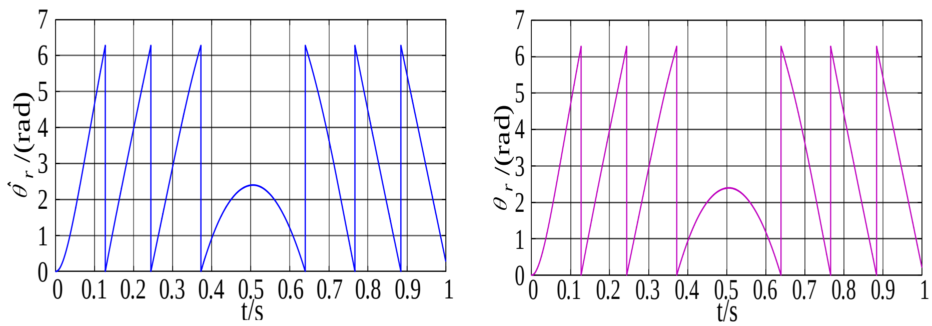

(**a**) actual rotor position (**b**) estimated rotor position

Figure 25. Rotor position waveform.

Figure 26 shows the speed estimated value and actual value change curve. It can be observed that this detection method can also track the actual speed of the rotor very well at low speeds, and has a good dynamic tracking performance.

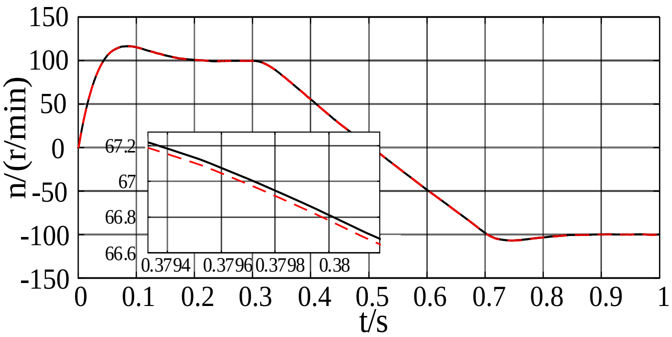

Figure 26. Speed waveform.

The PI controller used in the sensorless tracking is a one-degree-of-freedom controller. The parameter adjustment of the PI controller will affect the tracking performance and anti-disturbance performance of the system at the same time. If the parameters are set according to the optimal anti-interference performance, the system tracking performance will deteriorate. If the parameters are set according to the optimal tracking performance, the anti-interference performance will deteriorate. Therefore, the design and parameter tuning of conventional PI controllers are usually solved by compromise or trial and error. The valve position control system has high requirements on the speed response of the control system, which is very sensitive to overshoot and does not allow overshoot. Therefore, a control system based on a two-degree-of-freedom (2-DOF) and position sensorless algorithm is studied.

5. Two-Degree-of-Freedom Control Strategy

Combining the position sensorless control theory described above with the 2-DOF control, a vector control system based on 2-DOF and position sensorless algorithm can be designed. It can not only have strong anti-interference and speed control ability, but also has a certain adaptive ability, solves the problem of speed overshoot, and achieves smooth transition of the valve transient process.

In order to solve the problem that the traditional PI control cannot meet the requirements of speed overshoot and response rapidity, the 2-DOF control strategy is proposed to design the speed loop PI controller.

5.1. 2-DOF Controller

For the speed loop controller, the tracking performance and anti-disturbance performance of the system are optimized, respectively.

Figure 27 is a 2-DOF control with set-value filtering, where v is the control input, w is the outer disturbance input, *kp* and *ki* are the gains of proportional and integral parts, δ_n is the external noise input. H(s) is the compensation link and C(s) is the internal model controller. The transfer function of the control system under input is Φr(s), and the transfer function under disturbance is Φ_d(s), which is a high-frequency signal. The transfer function under measurement noise is Φ_n(s).

$$\Phi_r(s) = \frac{x(s)}{v(s)} = \frac{H(s)C(s)P(s)}{1 + C(s)P(s)} \tag{32}$$

$$\Phi_d(s) = \frac{x(s)}{w(s)} = \frac{P(s)}{1 + C(s)P(s)} \tag{33}$$

$$\Phi_n(s) = \frac{x(s)}{\delta_n(s)} = \frac{C(s)P(s)}{1 + C(s)P(s)} \tag{34}$$

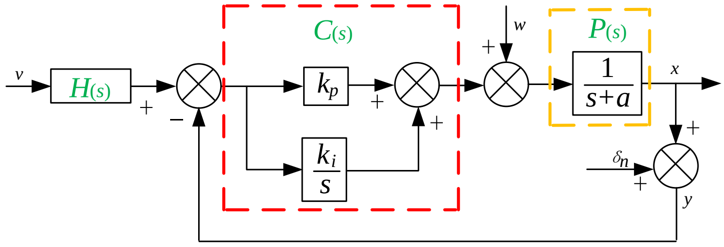

Figure 27. 2-DOF control with set-value filtering.

The system model $P(s)$ is determined, so the anti-interference performance and noise-measurement performance of the system are only related to $C(s)$, while the tracking performance of the system is not only related to $C(s)$, but also to $H(s)$. Among the three transfer functions $\Phi_r(s)$, $\Phi_d(s)$, and $\Phi_n(s)$, two transfer functions can be adjusted independently, so the system is a 2-DOF control system. When designing a 2-DOF control system, the system should first meet the requirements of anti-interference performance and suppression of measurement noise performance by designing C(s), which is the advantage of the 2-DOF control system.

The output of the 2-DOF PI control system with setting value filtering is:

$$\begin{aligned} x(s) &= \tfrac{H(s)C(s)P(s)}{1+C(s)P(s)}v(s) + \tfrac{P(s)}{1+C(s)P(s)}w(s) - \tfrac{C(s)P(s)}{1+C(s)P(s)}\delta_n(s) \\ &= \tfrac{(k_ps+k_i)H(s)}{s^2+(k_p+a)s+k_i}v(s) + \tfrac{s}{s^2+(k_p+a)s+k_i}w(s) \\ &-\tfrac{k_ps+k_i}{s^2+(k_p+a)s+k_i}\delta_n(s) \end{aligned} \tag{35}$$

In particular, when a = 0, the output of the control system can be simplified as:

$$\begin{aligned} x(s) &= \tfrac{(k_ps+k_i)H(s)}{s^2+k_ps+k_i}v(s) + \tfrac{s}{s^2+k_ps+k_i}w(s) \\ &-\tfrac{k_ps+k_i}{s^2+k_ps+k_i}\delta_n(s) \end{aligned} \tag{36}$$

From the above analysis, it can be seen that the two-degree-of-freedom PI controller first designs PI control parameters through the requirements of anti-disturbance performance, and then designs function $H(s)$ through the requirements of tracking performance. Adjusting the tracking performance by $H(s)$ does not affect the disturbance rejection performance.

It can be seen from Equation (36) that in order to make the system track without error under time-varying setting, the transfer function of the system under input can be designed as:

$$\Phi_r(s) = \frac{x(s)}{v(s)} = \frac{(k_ps+k_i)H_1(s)}{s^2+k_ps+k_i} = 1 \tag{37}$$

At this time, the corresponding set-valued filtering function H_1 (s) is:

$$H_1(s) = \frac{s^2+k_ps+k_i}{k_ps+k_i} \tag{38}$$

In order to make the step response of the system without overshoot, the transfer function of the system under input can be designed as a first-order or second-order low-pass filter.

$$\begin{aligned} \Phi_r(s) &= \tfrac{x(s)}{v(s)} = \tfrac{(k_ps+k_i)H_2(s)}{s^2+k_ps+k_i} \\ &= \tfrac{mk_p}{s+mk_p} or \tfrac{mk_ps+k_i}{s^2+k_ps+k_i} \end{aligned} \tag{39}$$

The corresponding set-valued filter function H_2(s) is:

$$H_2(s) = \frac{m(s^2 + k_p s + k_i)}{s^2 + (mk_p + k_i/k_p)s + mk_i} or \frac{mk_p s + k_i}{k_p s + k_i} \tag{40}$$

where m is a positive constant.

5.2. Simulation Analysis of 2-DOF Control

In order to verify the effectiveness of the new system, its step-response and anti-disturbance performance are analyzed. The sampling period of the speed loop and the current loop and the calculation step of the system are both 0.02 ms.

Take m = 0, ω_n is 30, 35, and 40, respectively, and ω_n is the speed loop bandwidth. The step is set to 100 rpm, and the waveform at no-load starting is shown in Figure 28.

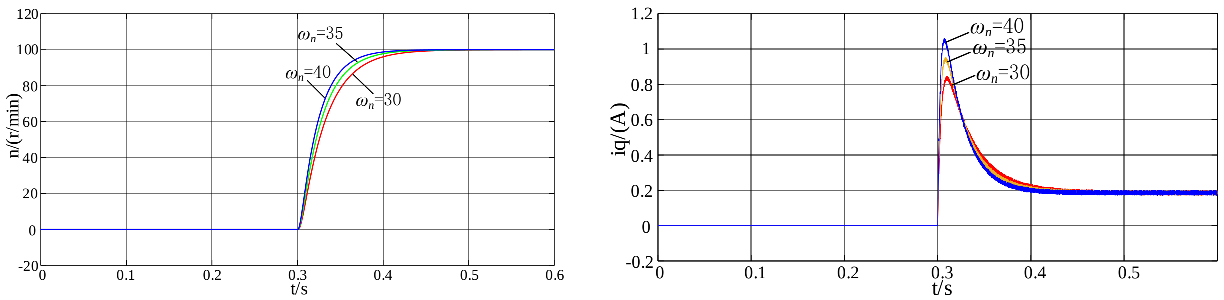

(**a**) No-load speed waveform (**b**) No-load current waveform

Figure 28. Step response under different ω_n values.

It can be seen from Figure 28 that the speed waveform is no longer in overshoot and has faster tracking than Figures 21 and 26. With the increase in the speed loop bandwidth, the faster the system response speed, and the better the speed tracking performance.

Take ω_n = 60, m is 0, 0.5 and 1, respectively. The step is set to 100 rpm, and the waveform at no-load starting is shown in Figure 29.

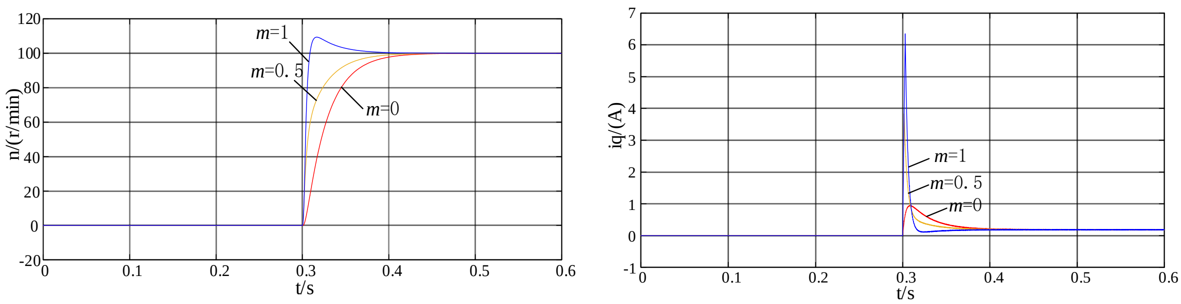

(**a**) No-load speed waveform (**b**) No-load current waveform

Figure 29. Step response under different m values.

The simulation results show that the designed 2-DOF PI control can effectively reduce the overshoot of the speed, and improve the speed tracking performance and the anti-disturbance performance of the system. The smaller the m value, the smaller the overshoot. With an increase in m value, the overshoot increases gradually. When m is 1, it is a sensorless waveform without 2-DOF control. Therefore, it can be concluded that the position sensorless control based on 2-DOF further improves the anti-load disturbance performance of the system, and can achieve fast response and no overshoot control of the speed. The correctness and effectiveness of the proposed control strategy are verified.

6. Experimental Test

In this paper, TMS320F28335 is selected as the DSP product for motion control. The control algorithm model that can automatically generate code is established on the MATLAB/Simulink platform, and the functions of the hardware system are tested and corrected. The vector control system based on 2-DOF and the position sensorless algorithm proposed in this paper is verified by experiments.

The variation curve of the calculated and measured rotor position at 1.2 times the rated speed is shown in Figure 30.

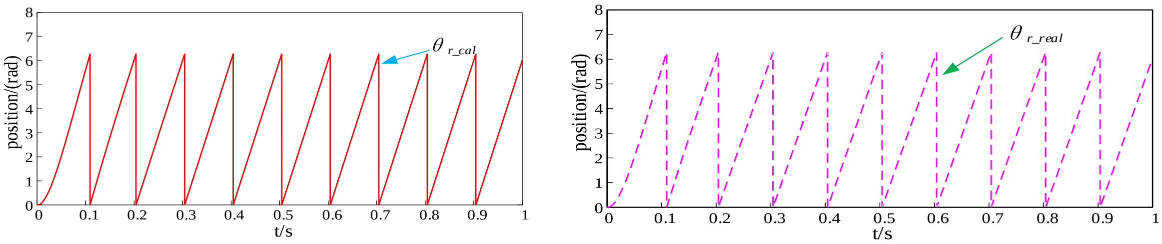

(**a**) Calculated rotor position curve (**b**) Measured rotor position curve

Figure 30. Rotor position waveform variation.

The step load disturbance is taken as an example to verify the anti-disturbance performance of the system. Firstly, 100 rpm is given to make the motor run without load, and then the influence of loading and unloading on speed fluctuation is tested. The loading and unloading curves are shown in Figure 31.

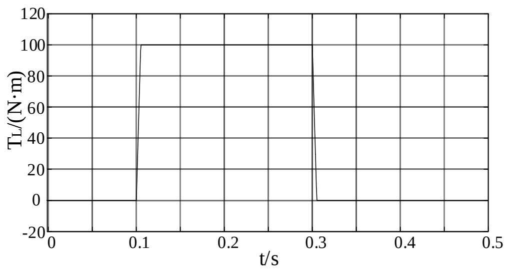

Figure 31. Load curve diagram.

Taking the unloading experiment as the assessment target, the 2-DOF control is systematically analyzed. Take m = 0, ω_n is 30, 35 and 40, respectively, and the speed response curve is shown in Figure 32a. Taking ω_n = 60, m is 0, 0.5, and 1, respectively, the speed response curve is shown in Figure 32b.

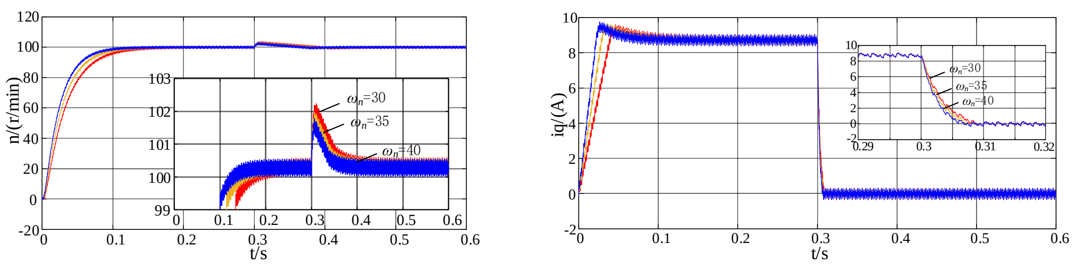

(**a**) Speed waveform during unloading (**b**) Current waveform during unloading

Figure 32. Unloading dynamic response under different ωn values.

It can be observed from Figures 32 and 33 that the anti-disturbance performance of the 2-DOF control system is only related to ω_n and independent of m. In summary, the tracking performance of the 2-DOF controller with set-value filtering is affected by ω_n and m at the same time, and the anti-interference performance is only affected by ω_n. It is proved that the vector control system based on 2-DOF and sensorless algorithm has good tracking performance and anti-interference performance, and has strong engineering practicability.

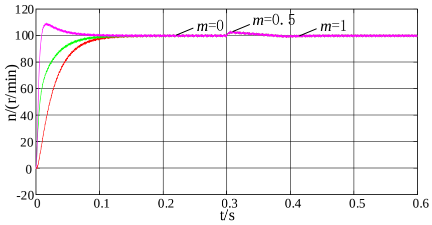

(**a**) Speed waveform during unloading

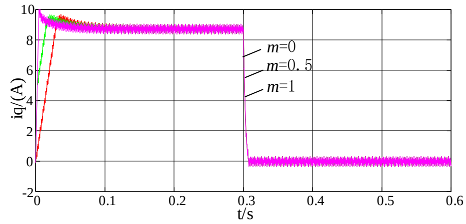

(**b**) Current waveform during unloading

Figure 33. Unloading dynamic response under different *m* values.

The experimental results show that the system can achieve accurate positioning and e fast response of the speed without overshoot, which meets the performance requirements of the servo system. The vector control system based on 2-DOF control and a sensorless algorithm has great improvements with regard to high precision, fast response, and strong robustness, which can enhance the system stability and the static as well as dynamic properties of the CEV-PMSM system significantly.

Figure 34 shows the main components and the experimental platform of CEV-PMSM.

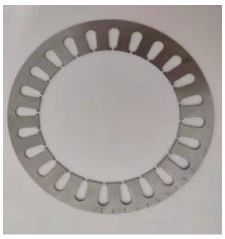

(**a**)

(**b**)

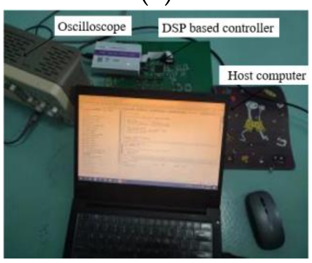

(**c**)

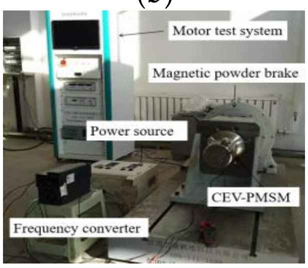

(**d**)

Figure 34. Experimental platform. (**a**) Stator lamination. (**b**) Stator canned sleeve. (**c**) Control platform. (**d**) Experimental platform for the CEV-PMSM.

7. Conclusions

This article introduces the new topology of CEV-PMSM, and analyzes the integrated structure and operating characteristics in detail. Afterwards, as an original contribution, the new MTPA model considering the canned sleeve parameters is derived for CEV-PMSM. On the basis, the vector control system based on 2-DOF and position sensorless algorithm is developed. Finally, experiments were conducted to verify the control performance of the system. The specific conclusions are as follows.

(1) The new MTPA control equation is deduced theoretically, and compared with the $i_d = 0$ control and the ideal MTPA control to analyze the influence of canned sleeve parameters on performance. The results show that the branch resistance introduced

by the canned sleeve increases the harmonic content of the stator current and more realistically reflects the variation of the current and torque waveforms under non-ideal conditions;

(2) We analyzed the mathematical model and extraction process of the rotor position signal under high-frequency rotating voltage in detail. It is proved that the sensorless control of the CEV-PMSM can obtain accurate position and speed tracking performance;

(3) The tracking performance of the 2-DOF controller with set-value filtering is affected by ω_n and m at the same time, and the anti-interference performance is only affected by ω_n. The vector control system based on 2-DOF control and sensorless algorithm can effectively improve the system dynamic and static performance, which has certain research value and guiding significance.

Author Contributions: Q.W. wrote the paper; W.L. supervised all processes; G.F. analyzed the data; B.Z. checked paper format. All authors have read and agreed to the published version of the manuscript.

Funding: This research received no external funding.

Conflicts of Interest: The authors declare no conflict of interest.

References

1. Noergaard, C.; Bech, M.M.; Christensen, J.H.; Andersen, T.O. Modeling and Validation of Moving Coil Actuated Valve for Digital Displacement Machines. *IEEE Trans. Ind. Electron.* **2018**, *65*, 8749–8757. [CrossRef]
2. YKim, H.; Lee, J.H. Optimum Design of ALA-SynRM for Direct Drive Electric Valve Actuator. *IEEE Trans. Magn.* **2017**, *53*, 1–4.
3. Gao, X.M.; Wang, X.F.; Wei, Z.C. Design and control of high-capacity and low-speed doubly fed start-up permanent magnet synchronous motor. *IET Electr. Power Appl.* **2018**, *12*, 1350–1356. [CrossRef]
4. Hwang, K.Y.; Song, B.K.; Kwon, B.I. Asymmetric dual winding three-phase PMSM for fault tolerance of overheat in electric braking system of autonomous vehicle. *IET Electr. Power Appl.* **2019**, *13*, 1891–1898. [CrossRef]
5. Ishikawa, T.; Seki, Y.; Kurita, N. Analysis for Fault Detection of Vector-Controlled Permanent Magnet Synchronous Motor with Permanent Magnet Defect. *IEEE Trans. Magn.* **2013**, *49*, 2331–2334. [CrossRef]
6. Shinohara, A.; Inoue, Y.; Morimoto, S.; Sanada, M. Direct Calculation Method of Reference Flux Linkage for Maximum Torque per Ampere Control in DTC-Based IPMSM Drives. *IEEE Trans. Power Electron.* **2017**, *32*, 2114–2122. [CrossRef]
7. Accetta, A.; Cirrincione, M.; Piazza, M.C.D.; Tona, G.L.; Luna, M.; Pucci, M. Analytical Formulation of a Maximum Torque per Ampere (MTPA) Technique for SynRMs Considering the Magnetic Saturation. *IEEE Trans. Ind. Appl.* **2020**, *56*, 3846–3854. [CrossRef]
8. Feng, G.; Lai, C.; Han, Y.; Kar, N.C. Fast Maximum Torque Per Ampere (MTPA) Angle Detection for Interior PMSMs Using Online Polynomial Curve Fitting. *IEEE Trans. Power Electron.* **2022**, *37*, 2045–2056. [CrossRef]
9. Inoue, T.; Inoue, Y.; Morimoto, S.; Sanada, M. Mathematical Model for MTPA Control of Permanent-Magnet Synchronous Motor in Stator Flux Linkage Synchronous Frame. *IEEE Trans. Ind. Appl.* **2015**, *51*, 3620–3628. [CrossRef]
10. Wang, J.; Huang, X.; Yu, D.; Chen, Y.Z.; Zhang, J.; Niu, F.; Fang, Y.T.; Cao, W.; Zhang, H. An Accurate Virtual Signal Injection Control of MTPA for an IPMSM With Fast Dynamic Response. *IEEE Trans. Power Electron.* **2018**, *33*, 7916–7926. [CrossRef]
11. Sun, T.; Wang, J.; Chen, X. Maximum Torque Per Ampere (MTPA) Control for Interior Permanent Magnet Synchronous Machine Drives Based on Virtual Signal Injection. *IEEE Trans. Power Electron.* **2015**, *30*, 5036–5045. [CrossRef]
12. Liu, Q.; Hameyer, K. High-Performance Adaptive Torque Control for an IPMSM with Real-Time MTPA Operation. *IEEE Trans. Energy Convers.* **2017**, *32*, 571–581. [CrossRef]
13. Li, K.; Wang, Y. Maximum Torque Per Ampere (MTPA) Control for IPMSM Drives Based on a Variable-Equivalent-Parameter MTPA Control Law. *IEEE Trans. Power Electron.* **2019**, *34*, 7092–7102. [CrossRef]
14. Xie, G.; Lu, K.; Dwivedi, S.K.; Rosholm, J.R.; Blaabjerg, F. Minimum-Voltage Vector Injection Method for Sensorless Control of PMSM for Low-Speed Operations. *IEEE Trans. Power Electron.* **2015**, *31*, 1785–1794. [CrossRef]
15. Zhao, S.; Wallmark, O.; Leksell, M. Low-Speed Sensorless Control with Reduced Copper Losses for Saturated PMSynRel Machines. *IEEE Trans. Energy Convers.* **2013**, *28*, 841–848. [CrossRef]
16. Matsui, N. Sensorless PM brushless DC motor drives. *IEEE Trans. Ind. Electron.* **1996**, *43*, 300–308. [CrossRef]
17. An, Q.; Zhang, J.; An, Q.; Shamekov, A. Quasi-Proportional-Resonant Controller Based Adaptive Position Observer for Sensorless Control of PMSM Drives Under Low Carrier Ratio. *IEEE Trans. Ind. Electron.* **2020**, *67*, 2564–2573. [CrossRef]
18. Gong, C.; Hu, Y.; Gao, J.; Wang, Y.; Yan, L. An Improved Delay-Suppressed Sliding-Mode Observer for Sensorless Vector-Controlled PMSM. *IEEE Trans. Ind. Electron.* **2020**, *67*, 5913–5923. [CrossRef]
19. Yang, H.; Yang, R.; Hu, W.; Huang, Z. FPGA-Based Sensorless Speed Control of PMSM Using Enhanced Performance Controller Based on the Reduced-Order EKF. *IEEE J. Emerg. Sel. Top. Power Electron.* **2021**, *9*, 289–301. [CrossRef]

20. Almarhoon, A.H.; Zhu, Z.Q.; Xu, P. Improved Rotor Position Estimation Accuracy by Rotating Carrier Signal Injection Utilizing Zero-Sequence Carrier Voltage for Dual Three-Phase PMSM. *IEEE Trans. Ind. Electron.* **2017**, *64*, 4454–4462. [CrossRef]
21. Zhou, X.; Zhou, B.; Wang, K. Position sensorless control for doubly salient electromagnetic machine with improved startup performance. *IEEE Trans. Ind. Electron.* **2020**, *67*, 1782–1791. [CrossRef]
22. Yang, S.; Hsu, Y. Full Speed Region Sensorless Drive of Permanent-Magnet Machine Combining Saliency-Based and Back-EMF-Based Drive. *IEEE Trans. Ind. Electron.* **2017**, *64*, 1092–1101. [CrossRef]
23. Yang, S.; Lorenz, R.D. Surface Permanent-Magnet Machine Self-Sensing at Zero and Low Speeds Using Improved Observer for Position, Velocity, and Disturbance Torque Estimation. *IEEE Trans. Ind. Appl.* **2012**, *48*, 151–160. [CrossRef]
24. Mendoza-Mondragón, F.; Hernández-Guzmán, V.M.; Rodríguez-Reséndiz, J. Robust speed control of permanent magnet synchronous motors using two-degrees-of-freedom control. *IEEE Trans. Ind. Electron.* **2018**, *65*, 6099–6108. [CrossRef]
25. Zhao, J.; Wang, L.; Dong, F.; He, Z.; Song, J. Robust high bandwidth current regulation for permanent magnet synchronous linear motor drivers by using two-degree-of-freedom controller and thrust ripple observer. *IEEE Trans. Ind. Electron.* **2019**, *67*, 1804–1812. [CrossRef]
26. Sun, X.; Chen, L.; Jiang, H.; Yang, Z.; Chen, J.; Zhang, W. High-performance control for a bearingless permanent-magnet synchronous motor using neural network inverse scheme plus internal model controllers. *IEEE Trans. Ind. Electron.* **2016**, *63*, 3479–3488. [CrossRef]
27. Mishra, I.; Tripathi, R.N.; Hanamoto, T. Two-degree-of-freedom (2DOF) Speed Control based FS-MPC for PMSM Drives. In Proceedings of the 2020 23rd International Conference on Electrical Machines and Systems (ICEMS), Hamamatsu, Japan, 24–27 November 2020; pp. 1230–1234.